Title	Evolution of the radio remnant of supernova 1987A: Morphological changes from day 7000
Author(s)	Ng, SCY; Zanardo, G; Potter, TM; Staveley-Smith, L; Gaensler, BM; Manchester, RN; Tzioumis, AK
Citation	The Astrophysical Journal, 2013, v. 777 n. 2, article no. 131
Issued Date	2013
URL	http://hdl.handle.net/10722/193599
Rights	The Astrophysical Journal. Copyright © Institute of Physics Publishing, Inc.

The Astrophysical Journal, 777:131 (10pp), 2013 November 10 doi:10.1088/0004-637X/777/2/131

EVOLUTION OF THE RADIO REMNANT OF SUPERNOVA 1987A: MORPHOLOGICAL CHANGES FROM DAY 7000

C.-Y. Ng[1], G. Zanardo[2], T. M. Potter[2], L. Staveley-Smith[2,3], B. M. Gaensler[3,4], R. N. Manchester[5], and A. K. Tzioumis[5]
[1] Department of Physics, The University of Hong Kong, Pokfulam Road, Hong Kong; ncy@bohr.physics.hku.hk
[2] International Centre for Radio Astronomy Research (ICRAR), The University of Western Australia, Crawley, WA 6009, Australia
[3] Australian Research Council, Centre of Excellence for All-sky Astrophysics (CAASTRO)
[4] Sydney Institute for Astronomy, School of Physics, The University of Sydney, NSW 2006, Australia
[5] CSIRO Astronomy and Space Science, Australia Telescope National Facility, Marsfield, NSW 1710, Australia
Received 2013 August 19; accepted 2013 September 10; published 2013 October 22

ABSTRACT

We present radio imaging observations of supernova remnant 1987A at 9 GHz, taken with the Australia Telescope Compact Array over 21 years from 1992 to 2013. By employing a Fourier modeling technique to fit the visibility data, we show that the remnant structure has evolved significantly since day 7000 (mid-2006): the emission latitude has gradually decreased such that the overall geometry has become more similar to a ring structure. Around the same time, we find a decreasing trend in the east–west asymmetry of the surface emissivity. These results could reflect the increasing interaction of the forward shock with material around the circumstellar ring, and the relative weakening of the interaction with the lower-density material at higher latitudes. The morphological evolution caused an apparent break in the remnant expansion measured with a torus model, from a velocity of 4600^{+150}_{-200} km s^{-1} between day 4000 and 7000 to 2400^{+100}_{-200} km s^{-1} after day 7000. However, we emphasize that there is no conclusive evidence for a physical slowing of the shock at any given latitude in the expanding remnant, and that a change of radio morphology alone appears to dominate the evolution. This is supported by our ring-only fits which show a constant expansion of 3890 ± 50 km s^{-1} without deceleration between days 4000 and 9000. We suggest that once the emission latitude no longer decreases, the expansion velocity obtained from the torus model should return to the same value as that measured with the ring model.

Key words: circumstellar matter – ISM: supernova remnants – radio continuum: ISM – shock waves – supernovae: individual (SN 1987A)

Online-only material: color figures

1. INTRODUCTION

The remarkable supernova (SN) 1987A in the Large Magellanic Cloud has enabled detailed studies of many fields in astrophysics from massive star evolution to the SN explosion mechanism to the earliest stage of supernova remnants (SNRs; see reviews in Immler et al. 2007). As well as being the brightest SN over the past 400 yr, SN 1987A was a highly unusual event. In particular, the progenitor was surrounded by a peculiar triple-ring nebula (Burrows et al. 1995), which could have resulted from a binary merger of the progenitor 20,000 yr prior to the explosion (Morris & Podsiadlowski 2007). Over the past decade, the remnant has undergone a major evolution since the shock collision with the inner equatorial ring, resulting in rapid brightening of the radio and soft X-ray emissions (see Zanardo et al. 2010; Helder et al. 2013 and references therein).

Radio emission of SNR 1987A is believed to be non-thermal synchrotron radiation emitted by energetic particles accelerated in shocks. Since the remnant emerged in mid-1990 (Turtle et al. 1990; Staveley-Smith et al. 1992), it has been monitored regularly at different frequencies using the Australia Telescope Compact Array (ATCA; see Staveley-Smith et al. 2007; Zanardo et al. 2010 and references therein). The flux density was found to have increased exponentially from day 5000 to 8000 with a progressively flatter spectrum (Zanardo et al. 2010), indicating increasingly efficient particle acceleration processes.

ATCA imaging observations at 9 GHz have been taken about twice a year since 1992 (Gaensler et al. 1997; Manchester et al. 2002; Ng et al. 2008, hereafter N08). With the source flux increase and various upgrades to the telescope, the remnant has been resolved at progressively higher frequencies, from 18 GHz to 36 GHz to 44 GHz to 94 GHz (Manchester et al. 2005; Potter et al. 2009; Zanardo et al. 2013; Lakićević et al. 2012), and also with very long baseline interferometry (VLBI) at 1.4 GHz and 1.7 GHz (Tingay et al. 2009; Ng et al. 2011a). The remnant shows similar structure at all these frequencies, and can be described as a thin shell with an asymmetric surface brightness distribution along the east–west direction. A thin-shell model was used to quantify the remnant structure in early studies (Staveley-Smith et al. 1993b; Gaensler et al. 1997). N08 developed a three-dimensional (3D) torus model that can capture the latitude extent of the emission and the east–west asymmetry. Fitting the torus model to observations between 1992 and 2008, a linear expansion of ∼4000 km s^{-1} was found up to day 8000, which is in contrast to the deceleration of the X-ray remnant observed around day 6000 (Racusin et al. 2009; Helder et al. 2013).

In this paper, we report on the latest evolution of the radio morphology of SNR 1987A up to day 9568 after the SN explosion, using 9 GHz ATCA imaging observations taken from 1992 January to 2013 May. The observations and Fourier modeling scheme are described in Sections 2 and 3, respectively, the modeling results are presented in Section 4, and we infer the remnant expansion rate in Section 5. The physical implications of the results are discussed in Section 6.

2. OBSERVATIONS AND DATA REDUCTION

Radio imaging of SNR 1987A at 9 GHz have been carried out for 21 yr since 1992 using ATCA in the 6 km array configuration,

Table 1
Observational Parameters for the Data Sets Used in This Study

Observing Date	Days since Supernova	Array Configuration	Center Frequency[a] (MHz)	Time on Source (hr)	Epoch Shown in Figure 1[b]
1992 Jan 14	1786	6B	8640	12	...
1992 Mar 20	1852	6A	8640	10	...
1992 Oct 21	2067	6C	8640, 8900	13	1992.9
1993 Jan 4	2142	6A	8640, 8900	9	1992.9
1993 Jan 5	2143	6A	8640, 8900	6	1992.9
1993 Jun 24	2313	6C	8640, 8900	8	1993.6
1993 Jul 1	2320	6C	8640, 8900	10	1993.6
1993 Oct 15	2426	6A	8640, 9024	17	1993.6
1994 Feb 16	2550	6B	8640, 9024	9	1994.4
1994 Jun 27–28	2681	6C	8640, 9024	21	1994.4
1994 Jul 1	2685	6A	8640, 9024	10	1994.4
1995 Jul 24	3073	6C	8640, 9024	12	1995.7
1995 Aug 29	3109	6D	8896, 9152	7	1995.7
1995 Nov 6	3178	6A	8640, 9024	9	1995.7
1996 Jul 21	3436	6C	8640, 9024	14	1996.7
1996 Sep 8	3485	6B	8640, 9024	13	1996.7
1996 Oct 5	3512	6A	8896, 9152	8	1996.7
1997 Nov 11	3914	6C	8512, 8896	7	1998.0
1998 Feb 18	4013	6A	8896, 9152	10	1998.0
1998 Feb 21	4016	6B	8512, 9024	7	1998.0
1998 Sep 13	4220	6A	8896, 9152	12	1998.9
1998 Oct 31	4268	6D	8502, 9024	11	1998.9
1999 Feb 12	4372	6C	8512, 8896	10	1999.7
1999 Sep 5	4577	6D	8768, 9152	11	1999.7
1999 Sep 12	4584	6A	8512, 8896	14	1999.7
2000 Sep 28	4966	6A	8512, 8896	10	2000.9
2000 Nov 12	5011	6C	8512, 8896	11	2000.9
2001 Nov 23	5387	6D	8768, 9152	8	2001.9
2002 Nov 19	5748	6A	8512, 8896	8	2003.0
2003 Jan 20	5810	6B	8512, 9024	9	2003.0
2003 Aug 1	6003	6D	8768, 9152	10	2003.6
2003 Dec 5	6129	6A	8512, 8896	9	2004.0
2004 Jan 15	6170	6A	8512, 8896	9	2004.0
2004 May 7	6283	6C	8512, 8896	9	2004.4
2005 Mar 25	6605	6A	8512, 8896	9	2005.2
2005 Jun 21	6693	6B	8512, 8896	9	2005.5
2006 Mar 28	6973	6C	8512, 8896	9	2006.2
2006 Jul 18	7085	6A	8512, 8896	9	2006.5
2006 Dec 8	7228	6B	8512, 9024	8	2006.9
2008 Jan 4	7620	6A	8512, 9024	11	2008.0
2008 Apr 23	7730	6A	8512, 8896	11	2008.3
2008 Oct 11	7901	6A	8512, 8896	11	2008.8
2009 Jun 6	8139	6A	9000	11	2009.4
2010 Jan 23	8370	6A	9000	11	2010.1
2010 Apr 11	8448	6A	9000	11	2010.3
2011 Jan 25	8737	6A	9000	11	2011.1
2011 Apr 22	8824	6A	9000	11	2011.3
2012 Jan 12	9089	6A	9000	11	2012.0
2012 Jun 5	9233	6D	9000	11	2012.4
2012 Sep 1	9321	6A	9000	10	2012.7
2013 Mar 7	9509	6A	9000	11	2013.2
2013 May 5	9568	6C	9000	11	2013.3

Notes.
[a] Since the CABB upgrade in mid-2009, data have been recorded over a 2 GHz bandwidth. However, in this analysis we used two 104 MHz sub-bands with center frequencies of 8.512 GHz and 8.896 GHz, for a consistency with the bandwidth of pre-CABB data.
[b] Some data sets have been averaged together to generate the corresponding images in Figure 1 for the listed epoch.

with a typical on-source time of ∼10 hr for each observation. In this paper, we analyze the remnant evolution in light of datasets recorded to date, which include recent observations taken since the Compact Array Broadband Backend (CABB; Wilson et al. 2011) upgrade in mid-2009. Table 1 lists the observation parameters. Pre-CABB observations were made in two frequencies with a usable bandwidth of 104 MHz each. While the bandwidth has been greatly increased to 2 GHz since the CABB upgrade, we restricted our analysis of the CABB data in two sub-bands only, with center frequencies of 8.512 GHz and

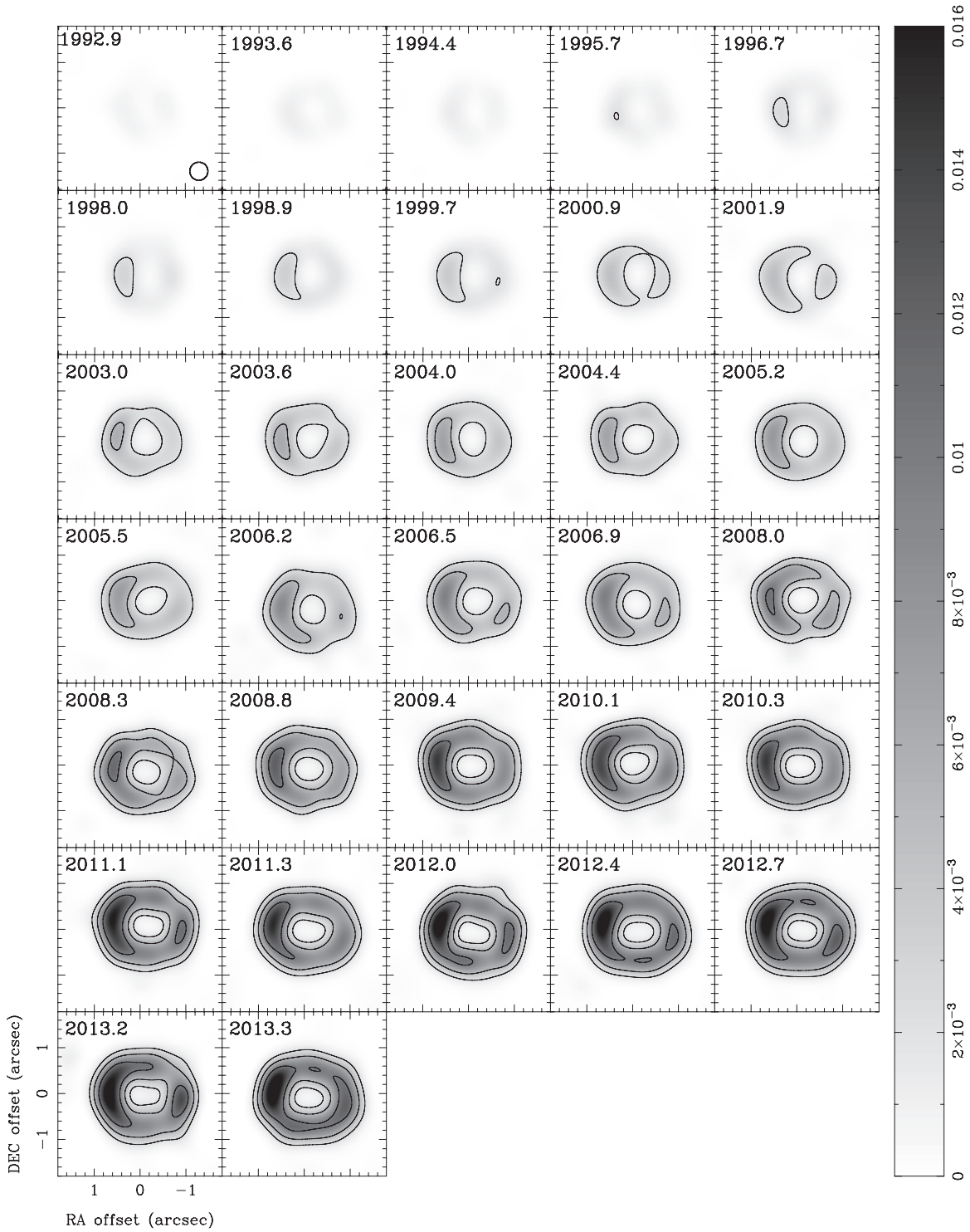

Figure 1. Super-resolved 9 GHz ATCA images of SN 1987A over the period 1992–2013. Some early epochs have been averaged to boost the signal-to-noise ratio (see Table 1). The gray scale is linear ranging from 0 to 16 mJy beam^{-1} and the contours are at levels of 2, 5, 10, and 15 mJy beam^{-1}. The synthesized beam, which has an FWHM of 0.″4, is shown in the first panel. The typical rms noise level is 0.05 mJy beam^{-1}.

8.896 GHz and a bandwidth of 104 MHz each, for a consistent comparison with previous data. Note that the data set taken on 2012 December 9 was affected by a storm, leaving only 6 hr of on-source time. It was not used in this study because the u–v sampling is inadequate for high-fidelity imaging, resulting in large rms noise in the final maps (0.5 mJy beam^{-1}).

All data were reduced using the MIRIAD package (Sault et al. 1995). After standard flagging and calibration, we employed self-calibration on data taken after 1996, when the source was detected with a high signal-to-noise ratio (see Gaensler et al. 1997; N08). The visibility data were averaged with five-minute intervals. The intensity maps formed from the visibility were deconvolved using a maximum entropy algorithm (Gull & Daniell 1978). We applied a super-resolution technique (Staveley-Smith et al. 1993a) by restoring the cleaned maps with a super-resolved circular beam of FWHM 0.″4 (see N08 for the details of the reduction procedure). The final maps have a typical rms noise of 0.05 mJy beam^{-1}. Figure 1 shows the

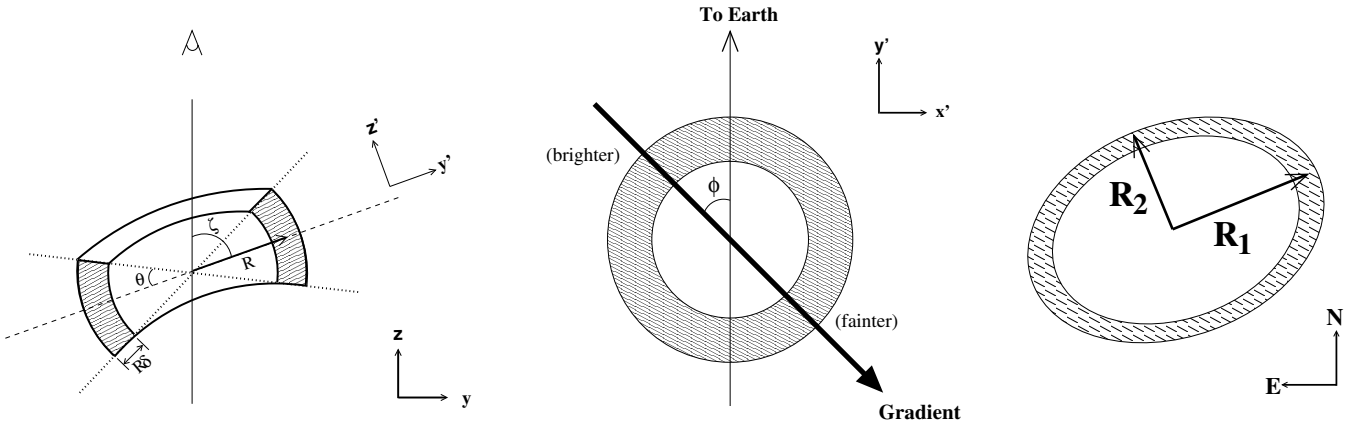

Figure 2. Illustration of the torus and ring models used in Fourier modeling. The left and middle panels are adopted from N08 to show the torus parameters: radius (R), half-opening angle (θ), inclination angle (ζ), thickness ($R\delta$), and position angle (ϕ) of the linear gradient in emissivity. The right panel shows the elliptical ring model in the image plane, with semi-major and semi-minor axes of R_1 and R_2, respectively. The ring's thickness is assumed to be negligible and the position angle is fixed during the fit.

resulting images. The remnant morphology can be described by a circular shell with two bright lobes. The eastern lobe is always brighter than the western lobe. Over the epochs, the remnant has brightened significantly and exhibited a clear expansion.

3. FOURIER MODELING

We followed previous studies (e.g., Staveley-Smith et al. 1993b; Gaensler et al. 1997; N08) to assess the remnant geometry in the u–v plane with the Fourier modeling technique. This can give more robust measurements than directly fitting a model in the image plane, since the Fourier domain is where the visibility data are taken and the measurement errors are uncorrelated. We employed two models in this study: a 3D torus as developed by N08 and a two-dimensional (2D) thin elliptical ring.

The torus model is illustrated in Figure 2. It is a truncated shell with eight fitting parameters: flux density, center position (right ascension and declination), radius, half-opening angle (θ), thickness (as a fraction of the radius), slope (in %), and direction (ϕ) of a linear gradient in the surface emissivity. The actual fitting was performed with a modified version of the MIRIAD task `UVFIT` (see N08 for details). As an update to the modeling, we employed the 9 GHz light curve reported by Zanardo et al. (2010) to account for the time-of-flight effect that causes the near side of the remnant to appear brighter than the far side. This gives slightly different results compared to N08, however, we emphasize that the differences are minimal and within the uncertainties.

Although N08 obtained confidence intervals of the fitting parameters using a simple bootstrapping technique, we note that the bootstrap samples may not be representative of the true population, and other techniques, such as subsample bootstrapping, are needed (see Kemball & Martinsek 2005). To avoid complications, we determined the confidence intervals from the covariance matrices. There are a few cases for which this method fails to give sensible results because the best-fit parameters are near the boundaries. We then estimated the confidence intervals by plotting out the χ^2 distribution.

In addition to the torus model, an elliptical ring model was also employed to compare with that used in X-ray studies (Racusin et al. 2009; Helder et al. 2013). As in the torus model, we included a linear gradient in the surface emissivity to account for the observed east–west asymmetry. The ring model has seven fitting parameters: flux density, center position, semi-major axis (R_1), semi-minor axis (R_2), and degree and direction of the gradient. The model is illustrated in Figure 2. Since the system is known have an inclination of $\sim$45° to the line of sight (e.g., Sugerman et al. 2005), we first tried fitting with the ring's aspect ratio fixed at $R_2/R_1 = 0.7$, but found that it gives slightly worse statistics than the torus fits. We then allowed both R_1 and R_2 to vary, which improves the results and gives comparable χ^2 values to the torus model. Same as the torus fits, confidence intervals of the best-fit parameters were determined from the covariance matrix.

4. RESULTS

The best-fit model parameters are listed in Tables 2 and 3. As an example, we show in Figure 3 images of the best-fit torus and ring models compared with the actual radio map taken on 2012 September 1, and the maps of the residual (i.e., data minus model) visibilities. The models have successfully captured the characteristic structure of the remnant. With one extra fitting parameter, the torus model provides slightly better fits to the data than the ring model. However, we cannot determine whether the difference in statistics is significant since the standard F-test does not apply here. As shown in Figure 3, the ring model underpredicts the flux density at the remnant center, but provides a better fit to the northern rim than the torus model.

Time evolution of the best-fit flux density, radius, opening angle, and degree of asymmetry, which is obtained from the slope of the gradient, are plotted in Figure 4. The torus radius increased linearly at the early epochs until a clear break at day $\sim$7000. After that, the expansion rate was significantly reduced. It is intriguing that around the same time when the break occurred, both θ and the asymmetry began to decrease. Since day $\sim$7500 the model flux density increases at a lower rate than the exponential fit given by Zanardo et al. (2010). For the other parameters not shown in the figure, the torus thickness is not well determined from the fits. As reported by N08, this is likely smaller than the resolution of the 9 GHz observations (see also Ng et al. 2011a). The direction of the linear gradient, which identifies the asymmetry of the surface brightness, remains mostly constant over the epochs.

For the ring model fit, it is clear from Figure 4(b) that R_1 is always smaller than the torus radius. When compared to the X-ray radius reported by Helder et al. (2013), R_1 has a similar

Table 2
Best-fit Parameters for the Torus Model with Statistical Uncertainties at a 68% Confidence Level

Day	Flux (mJy)	Radius ($''$)	Half-opening Angle ($^\circ$)	Thickness (%)	Asymmetry (%)	ϕ ($^\circ$)	χ^2_ν/dof[a]
1786	4.2 ± 0.2	0.60 ± 0.10	84^{+6}_{-20}	150 ± 50	70 ± 30	187 ± 16	1.8/2107
1852	4.0 ± 0.3	0.62 ± 0.05	80 ± 10	100 ± 50	100_{-60}	180^{+10}_{-30}	3.7/1642
2067	5.73 ± 0.12	0.62 ± 0.05	33 ± 4	175 ± 25	81 ± 7	121 ± 6	4.3/3602
2142	5.32 ± 0.14	0.65 ± 0.02	44 ± 2	172 ± 10	96 ± 3	114 ± 7	17/2702
2143	5.7 ± 0.2	0.64 ± 0.01	0^{+12}	0^{+20}	40 ± 8	108 ± 6	16/1392
2313	6.73 ± 0.11	0.63 ± 0.01	34 ± 7	0^{+20}	40 ± 5	94 ± 14	3.6/2902
2320	7.04 ± 0.13	0.67 ± 0.02	37 ± 7	44^{+15}_{-20}	38 ± 5	95 ± 13	4.5/2962
2426	6.65 ± 0.10	0.69 ± 0.01	55 ± 4	33^{+10}_{-16}	42 ± 5	85 ± 12	5.2/4372
2550	6.63 ± 0.15	0.64 ± 0.04	26 ± 5	175 ± 20	80 ± 6	108 ± 5	7.5/2992
2681	8.41 ± 0.08	0.67 ± 0.01	48 ± 3	18^{+10}_{-17}	33 ± 4	92 ± 10	6.0/6142
2685	8.11 ± 0.10	0.66 ± 0.01	54 ± 4	0^{+14}	38 ± 6	113 ± 12	5.7/3256
3073	11.11 ± 0.12	0.67 ± 0.01	34 ± 5	46 ± 14	40 ± 3	93 ± 8	5.6/2662
3109	9.7 ± 0.1	0.64 ± 0.02	18^{+10}_{-18}	0^{+15}	42 ± 2	88 ± 7	17/1598
3178	11.71 ± 0.09	0.685 ± 0.007	45 ± 2	0^{+10}	39 ± 2	103 ± 7	4/3442
3436	15.17 ± 0.09	0.705 ± 0.005	47 ± 2	24 ± 11	42 ± 2	95 ± 4	4.9/4337
3485	15.42 ± 0.08	0.707 ± 0.005	51 ± 2	1^{+10}	43 ± 2	102 ± 5	5.2/4702
3512	15.43 ± 0.12	0.708 ± 0.006	53 ± 2	0^{+18}	42 ± 3	94 ± 6	3.3/2632
3914	17.57 ± 0.14	0.694 ± 0.007	42 ± 3	0^{+10}	38 ± 3	111 ± 7	2.4/1272
4013	19.09 ± 0.10	0.754 ± 0.005	46.4 ± 1.4	0^{+5}	45.1 ± 1.5	104 ± 4	3.0/2830
4016	18.72 ± 0.10	0.745 ± 0.006	51 ± 2	0^{+5}	46 ± 2	103 ± 5	3.1/2512
4220	20.20 ± 0.09	0.729 ± 0.004	43.4 ± 1.3	2^{+13}_{-2}	37.6 ± 1.3	100 ± 3	2.2/2955
4268	21.78 ± 0.13	0.736 ± 0.006	40 ± 2	28 ± 8	38 ± 2	107 ± 4	7.3/3862
4372	22.94 ± 0.10	0.727 ± 0.005	37 ± 2	23 ± 9	37.4 ± 1.5	114 ± 3	3.6/3532
4577	23.89 ± 0.14	0.757 ± 0.007	40 ± 2	21 ± 6	39 ± 2	103 ± 4	7.0/3442
4584	25.23 ± 0.07	0.747 ± 0.003	42.0 ± 1.0	0^{+5}	38.5 ± 1.0	109 ± 2	2.9/4222
4966	29.45 ± 0.06	0.764 ± 0.002	40.8 ± 0.6	0^{+5}	39.5 ± 0.6	108.3 ± 1.3	1.3/50689
5011	32.97 ± 0.07	0.775 ± 0.002	44.1 ± 0.7	1^{+5}_{-1}	40.1 ± 0.6	104.9 ± 1.4	1.4/50531
5387	34.11 ± 0.08	0.790 ± 0.003	41.4 ± 0.8	0^{+3}	41.5 ± 0.7	107.8 ± 1.5	1.6/39604
5748	41.68 ± 0.07	0.811 ± 0.002	43.8 ± 0.5	0^{+2}	40.2 ± 0.5	103.1 ± 1.2	1.3/38992
5810	42.46 ± 0.07	0.815 ± 0.002	42.9 ± 0.5	1^{+4}_{-1}	42.8 ± 0.6	117.4 ± 1.0	1.6/46012
6003	46.50 ± 0.07	0.815 ± 0.002	39.6 ± 0.5	0^{+2}	38.4 ± 0.5	101.2 ± 1.1	1.6/44992
6129	52.82 ± 0.08	0.833 ± 0.002	42.7 ± 0.5	0^{+2}	42.1 ± 0.4	107.7 ± 1.1	1.3/46012
6170	54.05 ± 0.08	0.831 ± 0.002	42.2 ± 0.5	0^{+2}	38.8 ± 0.4	107.8 ± 1.1	1.5/43672
6283	53.63 ± 0.07	0.829 ± 0.001	39.6 ± 0.4	0^{+2}	38.8 ± 0.4	107.7 ± 0.9	1.5/44842
6605	61.36 ± 0.10	0.843 ± 0.002	38.2 ± 0.5	0^{+2}	39.1 ± 0.5	109.0 ± 1.1	2.9/42892
6693	62.69 ± 0.08	0.858 ± 0.001	43.0 ± 0.4	0^{+3}	35.9 ± 0.4	101.5 ± 1.0	1.5/38992
6973	73.81 ± 0.08	0.880 ± 0.001	44.6 ± 0.3	0^{+2}	42.1 ± 0.4	117.4 ± 0.7	1.5/40357
7085	77.19 ± 0.08	0.872 ± 0.001	39.3 ± 0.3	0^{+1}	39.8 ± 0.3	111.8 ± 0.6	1.5/29112
7228	82.51 ± 0.08	0.874 ± 0.001	40.0 ± 0.3	0^{+1}	39.4 ± 0.3	109.1 ± 0.7	1.4/35677
7620	93.61 ± 0.09	0.893 ± 0.001	42.7 ± 0.3	0^{+4}	38.9 ± 0.3	105.1 ± 0.6	1.3/42892
7730	98.98 ± 0.08	0.8905 ± 0.0008	36.2 ± 0.2	0^{+1}	36.3 ± 0.2	109.4 ± 0.5	1.6/40942
7901	107.73 ± 0.08	0.8916 ± 0.0007	35.8 ± 0.2	0^{+2}	35.9 ± 0.2	109.1 ± 0.4	1.5/44452
8139	121.59 ± 0.08	0.9095 ± 0.0006	37.6 ± 0.1	0^{+4}	32.0 ± 0.1	104.4 ± 0.4	0.5/278820
8370	128.07 ± 0.08	0.9142 ± 0.0006	36.6 ± 0.2	0^{+1}	33.4 ± 0.2	105.4 ± 0.4	0.8/254302
8448	132.59 ± 0.07	0.9109 ± 0.0008	33.5 ± 0.2	12 ± 3	28.7 ± 0.1	103.4 ± 0.4	0.9/301177
8737	142.25 ± 0.07	0.9185 ± 0.0005	32.8 ± 0.1	0^{+2}	29.8 ± 0.1	104.2 ± 0.4	0.6/251707
8824	136.58 ± 0.08	0.9169 ± 0.0008	28.4 ± 0.2	1^{+3}_{-1}	26.9 ± 0.1	105.7 ± 0.4	0.7/241327
9089	155.92 ± 0.06	0.9251 ± 0.0005	30.5 ± 0.1	0^{+1}	25.8 ± 0.1	102.3 ± 0.4	1.1/265987
9233	161.00 ± 0.06	0.9290 ± 0.0006	28.8 ± 0.1	1^{+2}_{-1}	25.8 ± 0.1	102.4 ± 0.3	1.0/301177
9321	165.62 ± 0.05	0.9304 ± 0.0003	29.1 ± 0.1	0^{+1}	23.5 ± 0.1	98.4 ± 0.3	0.9/284272
9509	168.68 ± 0.05	0.9467 ± 0.0003	31.7 ± 0.1	0^{+1}	26.7 ± 0.1	97.8 ± 0.2	1.4/288550
9568	176.01 ± 0.04	0.9378 ± 0.0002	28.6 ± 0.1	0^{+1}	18.4 ± 0.1	111.6 ± 0.3	1.3/283341

Notes. [a] Before 2000, all 26 frequency channels in the data were averaged into one band of effective bandwidth 208 MHz to boost the signal; between 2000 and 2009, 26 Hanning-smoothed channels, each of width 8 MHz were used in the fit; since mid-2009, after the installation of the Compact Array Broadband Backend (CABB), 208 channels in the same frequency range were extracted, each of width 1 MHz. Since 2012, the ATCA sensitivity has improved by ∼40% as a result of the installation of new receivers.

size between days 6000 and 7500, and it is larger after day 7500. Over time, R_1 increases linearly without obvious deceleration. In contrast, R_2 exhibits a break around day 7000, as did the torus radius. This results in a decrease in the ratio R_2/R_1, which shows a remarkably similar trend to that of θ (Figure 4(c)). The ring and torus fits give nearly identical flux densities and both suggest a decreasing trend in the degree of asymmetry since day ∼7500. For completeness, we also show in Figure 5 the best-fit R_1 and R_2 from the ring fitting with a fixed aspect ratio. We obtained larger R_1 and smaller R_2 as compared to the ring fit with varying aspect ratio, and there is a hint of a break in the expansion around day 7500.

Table 3
Best-fit Parameters for the Ring Model with Statistical Uncertainties at a 68% Confidence Level

Day	Flux (mJy)	Semi-major Axis (″)	Semi-minor Axis (″)	Asymmetry (%)	ϕ (°)	χ^2_ν/dof[a]
1786	3.70 ± 0.12	0.55 ± 0.03	0.50 ± 0.03	33 ± 16	141 ± 26	1.8/2108
1852	3.59 ± 0.14	0.53 ± 0.04	0.48 ± 0.04	25 ± 17	124 ± 46	3.7/1643
2067	5.17 ± 0.09	0.57 ± 0.02	0.49 ± 0.01	27 ± 5	105 ± 16	4.4/3603
2142	4.84 ± 0.11	0.53 ± 0.02	0.51 ± 0.02	17 ± 8	132 ± 29	17/2703
2143	5.62 ± 0.14	0.63 ± 0.03	0.44 ± 0.02	39 ± 8	94 ± 24	16/1393
2313	6.68 ± 0.09	0.57 ± 0.02	0.44 ± 0.01	34 ± 5	90 ± 15	3.6/2903
2320	6.87 ± 0.10	0.61 ± 0.02	0.47 ± 0.01	31 ± 4	92 ± 13	4.5/2963
2426	6.47 ± 0.08	0.56 ± 0.01	0.50 ± 0.01	28 ± 4	86 ± 9	5.2/4373
2550	6.12 ± 0.12	0.58 ± 0.02	0.54 ± 0.02	32 ± 6	117 ± 12	7.5/2993
2681	8.23 ± 0.06	0.58 ± 0.01	0.48 ± 0.01	26 ± 3	87 ± 8	6.0/6143
2685	7.94 ± 0.08	0.56 ± 0.01	0.49 ± 0.01	29 ± 4	109 ± 10	5.7/3257
3073	10.86 ± 0.10	0.62 ± 0.01	0.47 ± 0.01	33 ± 2	87 ± 8	5.6/2663
3109	9.73 ± 0.23	0.60 ± 0.01	0.50 ± 0.01	36 ± 8	92 ± 32	17/1599
3178	11.50 ± 0.07	0.601 ± 0.007	0.487 ± 0.006	32 ± 2	98 ± 6	4.0/3443
3436	14.76 ± 0.07	0.607 ± 0.005	0.495 ± 0.004	33 ± 1	94 ± 4	5.0/4338
3485	15.07 ± 0.07	0.598 ± 0.006	0.510 ± 0.004	33 ± 2	98 ± 4	5.2/4703
3512	15.06 ± 0.10	0.592 ± 0.007	0.508 ± 0.005	32 ± 2	91 ± 5	3.4/2633
3914	17.31 ± 0.12	0.624 ± 0.006	0.491 ± 0.007	33 ± 3	107 ± 7	2.4/1273
4013	18.53 ± 0.09	0.646 ± 0.005	0.527 ± 0.004	35.5 ± 1.2	99 ± 3	3.0/2831
4016	18.36 ± 0.09	0.632 ± 0.005	0.545 ± 0.006	35.8 ± 1.3	98 ± 4	3.1/2513
4220	19.76 ± 0.07	0.643 ± 0.004	0.509 ± 0.003	31.4 ± 1.0	96 ± 3	2.2/2956
4268	21.19 ± 0.11	0.656 ± 0.006	0.506 ± 0.005	31.1 ± 1.5	104 ± 4	7.4/3863
4372	22.43 ± 0.08	0.663 ± 0.004	0.500 ± 0.004	32.1 ± 1.2	111 ± 3	3.6/3533
4577	23.26 ± 0.12	0.674 ± 0.006	0.515 ± 0.005	32.7 ± 1.4	98 ± 4	7.1/3443
4584	24.69 ± 0.07	0.663 ± 0.003	0.521 ± 0.003	31.6 ± 0.8	103 ± 2	2.9/4223
4966	28.75 ± 0.05	0.681 ± 0.002	0.527 ± 0.002	32.9 ± 0.5	102 ± 1	1.3/50690
5011	32.03 ± 0.06	0.677 ± 0.002	0.531 ± 0.002	32.7 ± 0.5	100 ± 1	1.4/50532
5387	33.19 ± 0.07	0.694 ± 0.002	0.547 ± 0.002	34.0 ± 0.5	102 ± 1	1.6/39605
5748	40.56 ± 0.06	0.710 ± 0.002	0.564 ± 0.001	33.0 ± 0.4	97 ± 1	1.3/38993
5810	41.24 ± 0.06	0.723 ± 0.002	0.568 ± 0.002	34.8 ± 0.4	110 ± 1	1.6/46013
6003	45.35 ± 0.06	0.723 ± 0.002	0.561 ± 0.002	32.2 ± 0.4	94 ± 1	1.6/44993
6129	51.43 ± 0.07	0.733 ± 0.002	0.579 ± 0.002	34.7 ± 0.3	100 ± 1	1.3/46013
6170	52.63 ± 0.07	0.734 ± 0.001	0.577 ± 0.002	32.1 ± 0.3	102 ± 1	1.5/43673
6283	52.18 ± 0.06	0.743 ± 0.001	0.569 ± 0.001	32.8 ± 0.3	101 ± 1	1.5/44843
6605	59.86 ± 0.09	0.758 ± 0.002	0.586 ± 0.002	33.0 ± 0.4	101 ± 1	2.9/42893
6693	61.21 ± 0.07	0.7622 ± 0.0013	0.5979 ± 0.0013	30.1 ± 0.3	95 ± 1	1.5/38993
6973	71.33 ± 0.07	0.7743 ± 0.0011	0.6118 ± 0.0014	33.7 ± 0.3	110 ± 1	1.5/40358
7085	74.60 ± 0.07	0.7695 ± 0.0012	0.5939 ± 0.0011	32.6 ± 0.2	103 ± 1	1.6/29113
7228	80.53 ± 0.07	0.7825 ± 0.0009	0.6171 ± 0.0010	33.0 ± 0.2	101 ± 1	1.4/35678
7620	90.47 ± 0.08	0.7830 ± 0.0011	0.6208 ± 0.0009	31.8 ± 0.2	97 ± 1	1.4/42893
7730	96.36 ± 0.07	0.8058 ± 0.0008	0.6179 ± 0.0008	30.9 ± 0.2	102 ± 1	1.6/40943
7901	104.94 ± 0.06	0.8075 ± 0.0007	0.6220 ± 0.0007	30.8 ± 0.1	102 ± 0	1.5/44453
8139	117.73 ± 0.07	0.8241 ± 0.0006	0.6263 ± 0.0006	27.7 ± 0.1	97 ± 0	0.5/278821
8370	124.86 ± 0.07	0.8243 ± 0.0006	0.6428 ± 0.0007	28.6 ± 0.1	98 ± 0	0.8/254303
8448	129.50 ± 0.06	0.8406 ± 0.0005	0.6282 ± 0.0006	25.6 ± 0.1	94 ± 0	0.9/301178
8737	139.17 ± 0.06	0.8433 ± 0.0005	0.6430 ± 0.0005	26.2 ± 0.1	96 ± 0	0.7/251708
8824	133.95 ± 0.07	0.8582 ± 0.0006	0.6373 ± 0.0007	24.1 ± 0.1	96 ± 0	0.7/241328
9089	153.09 ± 0.05	0.8593 ± 0.0004	0.6438 ± 0.0005	23.1 ± 0.1	92 ± 0	1.1/265988
9233	157.94 ± 0.05	0.8698 ± 0.0004	0.6401 ± 0.0005	23.4 ± 0.1	93 ± 0	1.1/301178
9321	162.98 ± 0.05	0.8703 ± 0.0003	0.6527 ± 0.0004	21.5 ± 0.1	88 ± 0	0.9/284273
9509	165.10 ± 0.04	0.8761 ± 0.0003	0.6583 ± 0.0003	24.0 ± 0.1	88 ± 0	1.4/288551
9568	173.03 ± 0.04	0.8818 ± 0.0002	0.6574 ± 0.0003	16.2 ± 0.1	100 ± 0	1.4/283342

Notes. [a] Before 2000, all 26 frequency channels in the data were averaged into one band of effective bandwidth 208 MHz to boost the signal; between 2000 and 2009, 26 Hanning-smoothed channels, each of width 8 MHz were used in the fit; since mid-2009, after the installation of the Compact Array Broadband Backend (CABB), 208 channels in the same frequency range were extracted, each of width 1 MHz. Since 2012, the ATCA sensitivity has improved by ∼40% as a result of the installation of new receivers.

5. RATE OF EXPANSION

The torus fitting results shown in Figure 4(b) suggest a possible deceleration of the remnant. We therefore followed Racusin et al. (2009) to fit the radius evolution with a broken linear function. Only observations after day 4200 were used here, since we are most interested in the late evolution of the remnant. We note that the radius measurements in Table 2 have statistical uncertainties of the order of 0.″001, much smaller than the scatter from measurement to measurement. We therefore added in quadrature systematic uncertainties of 0.″005 to the measurements errors. This value was chosen to give a reduced

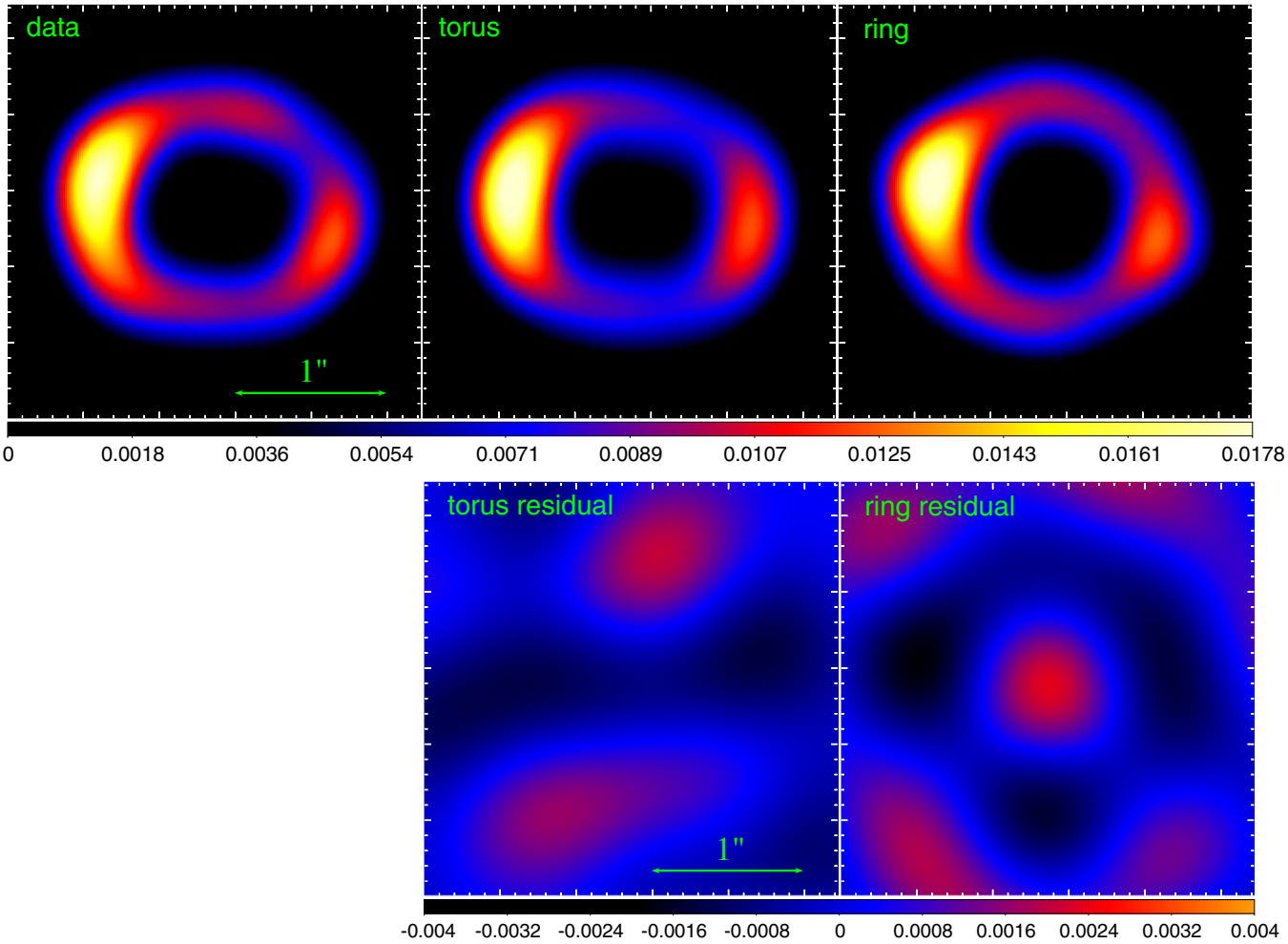

Figure 3. Radio image of SN 1987A at 9 GHz taken on 2012 September 1 (left) compared with images of the best-fit torus (middle) and elliptical ring (right) models. The lower panels show the maps of the residual (i.e., data minus model) visibilities for which no deconvolution has been applied. Note that the upper and lower panels have different color scales.

(A color version of this figure is available in the online journal.)

χ^2 value of about 1 for the broken linear fit. We have tried different values from 0 to 0.″05 and confirm that our results are independent of the choice.

Table 4 lists the best-fit expansion velocity and transition day. Uncertainties quoted are 68% confidence intervals determined using a bootstrapping technique (Efron & Tibshirani 1993) with 10,000 simulations. The break in the expansion of the torus model occurred on day 7000^{+200}_{-100}, and was the same as R_2 of the ring model (day 7000 ± 300). However, R_1 shows no breaks and a simple linear fit is statistically preferred. Finally, the ring fit with a constant aspect ratio suggests a somewhat later transition at day 7600 ± 200. At a source distance of 51.4 kpc (Panagia 1999), the torus fits suggest expansion velocities of $v_1 = 4600^{+150}_{-200}$ km s^{-1} and $v_2 = 2400^{+100}_{-200}$ km s^{-1} before and after the break, respectively. While v_1 is larger than the expansion rate 3890 ± 50 km s^{-1} of R_1, both values are consistent with the result of 4000 ± 400 km s^{-1} reported by N08. Similar to the torus radius, the expansion velocity of R_2 decreased by nearly 50%, from 3300 km s^{-1} to 1750 km s^{-1}, after the break.

6. DISCUSSION

Non-thermal radio emission from SNRs traces the particle acceleration in shocks. Theories suggest that the emission is generally distributed between the forward and reverse shocks (e.g., Jun & Norman 1996). When the shocks of SN 1987A travel outward and encounter the equatorial ring, we expect the radio-emitting region to have a complex structure in 3D (e.g., Suzuki et al. 1993; Luo et al. 1994; Blondin et al. 1996), with components from both high-latitude material above the equatorial plane and the ring itself. To characterize the remnant geometry, we have carried out Fourier modeling using a truncated-shell torus model and an elliptical thin ring model. Although both provide adequate fits to the data, we should note that these models are simple parameterizations of the remnant structure, and that the geometry inferred from the fitting is model-dependent and could be systematically biased. For instance, if the actual shape of the emission resembles a crescent torus (Plait et al. 1995), then the radius measurement obtained from our torus model would depend sensitively on θ.

One major discrepancy between the torus and ring models is the radius measurement. We find that the radius obtained from fitting a torus model is always larger than that from a ring model. This could be a projection effect due to differences in the model geometry or the emission at high latitudes, to which the torus model is more sensitive, being physically further away from the center. For the former, consider a thin spherical shell in 3D: in the image the emission would appear to peak inside the shell

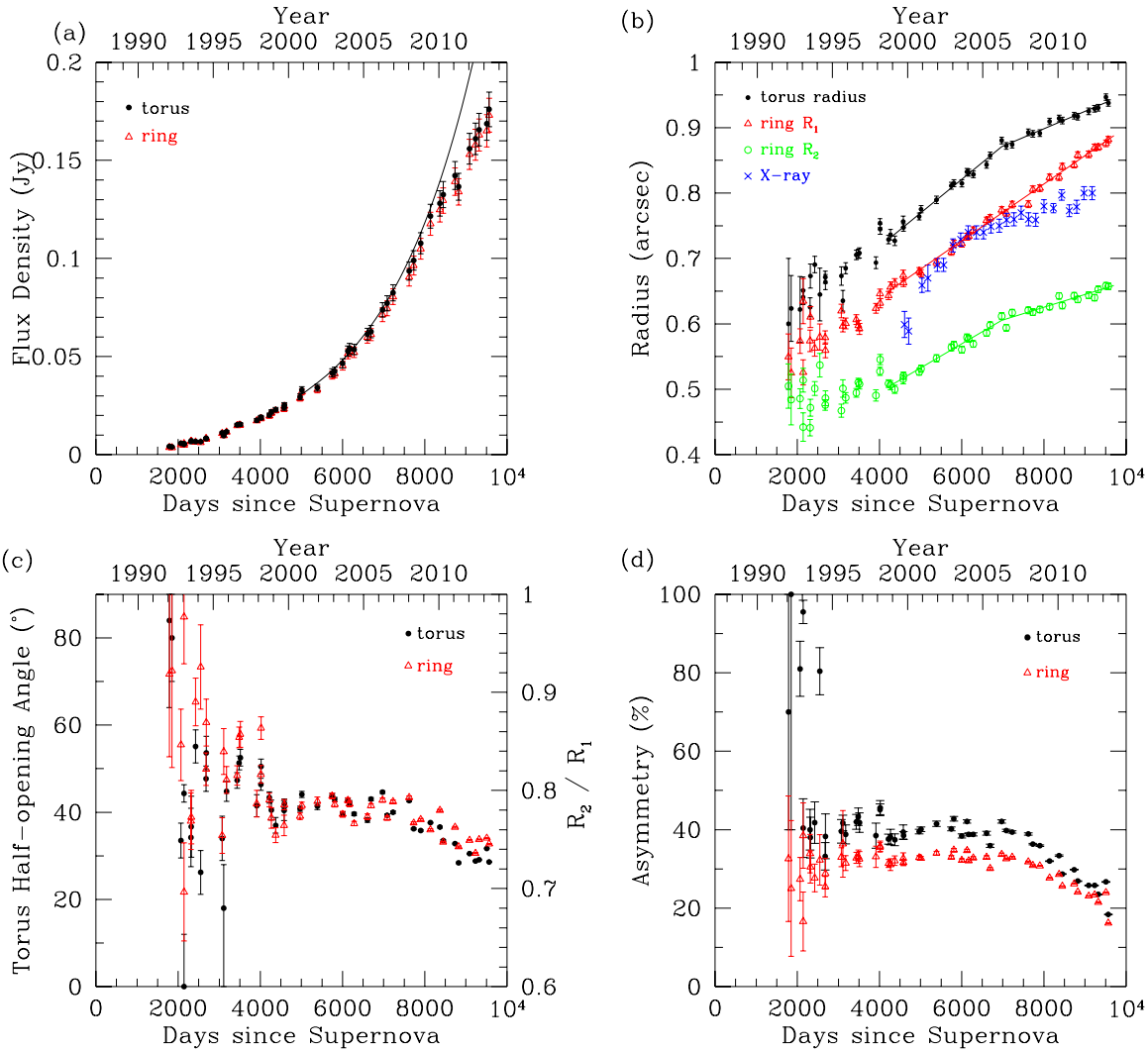

Figure 4. (a) Model flux densities at 9 GHz. Systematic uncertainties of 5% (Zanardo et al. 2013) are combined with the statistical uncertainties at a 68% confidence level. The solid line is the exponential fit from Zanardo et al. (2010). (b) Best-fit radius of the torus model and semi-major (R_1) and semi-minor (R_2) axes of the ring model, compared with the X-ray radius reported by Helder et al. (2013). Systematic uncertainties of 0.″005 are combined with the statistical uncertainties at 68% confidence level. The solid lines are the best-fit expansion rates in Table 4. (c) Best-fit torus half-opening angle θ compared with the ratio R_2/R_1 of the ring model. (d) Best-fit asymmetry in the surface brightness.

(A color version of this figure is available in the online journal.)

Table 4
Expansion of the Radio Remnant of SN 1987A Since Day 4200, with Uncertainties at a 68% Confidence Level

Model	Transition Day	v_1 (km s^{-1})	v_2 (km s^{-1})
Torus	7000^{+200}_{-100}	4600^{+150}_{-200}	2400^{+100}_{-200}
Ring semi-major axis[a]	...	3890 ± 50	...
Ring semi-minor axis	7000 ± 300	3300 ± 200	1750^{+150}_{-300}
Ring semi-major axis (aspect ratio fixed)[b]	7600 ± 200	3940 ± 70	2900 ± 100
Ring semi-minor axis (aspect ratio fixed)[b]	7600 ± 200	2710 ± 50	2000^{+60}_{-70}

Notes.
[a] A simple linear expansion is preferred over a broken linear fit.
[b] Expansion of the semi-major and semi-minor axes are linked as the ring's aspect ratio is fixed during the fit.

radius because of projection and the finite spatial resolution of the telescope. Hence, a 3D shell model would require a larger radius compared to a simple thin ring model. Our torus model varies between a shell and a ring depending on θ (see Figure 2). The projection effect is minimum at $\theta = 0$, where the torus reduces to a 2D ring, and increases with θ. Given that the best-fit θ is significantly greater than zero, the above discrepancy is not unexpected. Alternatively, the radio-emitting region could have a larger radius at higher latitudes than at the equatorial plane because the SN shock travels at a larger velocity in the

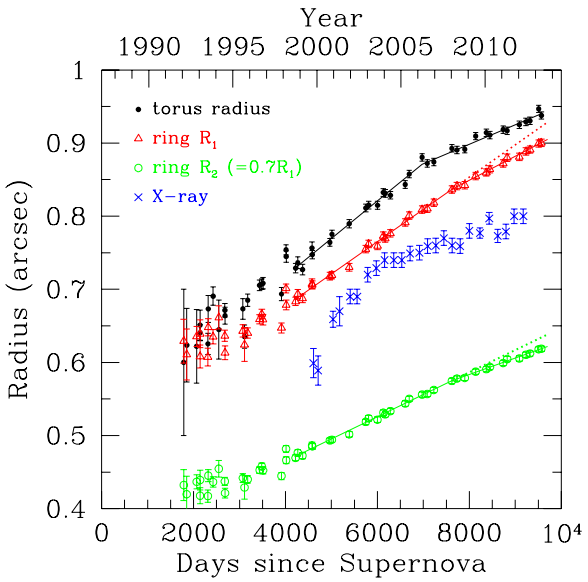

Figure 5. Same as Figure 4(b), but the aspect ratio of the ring model is fixed at $R_2/R_1 = 0.7$ according to the inclination of the system. To better illustrate the break in the expansion of R_1 and R_2, the dotted lines indicate the expansion without any breaks for a direct comparison.

(A color version of this figure is available in the online journal.)

low-density environment (Blondin et al. 1996). If this is the case, any 3D models sensitive to high-latitude emission, such as the torus model, will tend to give a larger radius. It is worth noting that in both scenarios above, there is a possible coupling between the torus radius and θ, and it could correspondingly impact the expansion measurement.

In previous studies, the reported radii of SNR 1987A in radio and X-rays show a 10% difference over day 5000–8000 (N08; Racusin et al. 2009). It was first pointed out by Gaensler et al. (2007) that the discrepancy may not be physical but due to different measuring techniques. This idea is similar to what we have discussed above. In particular, measurements from N08 were made with a torus model, while the X-ray results were obtained from ring fitting (Racusin et al. 2009; Helder et al. 2013). Gaensler et al. (2007) analyzed both radio and X-ray data taken in 2004 (day $\sim$ 6300) using a consistent method and showed that the SNR sizes agree to within 1%. Our results confirm their finding: R_1 from the ring model at this epoch is fully consistent with the X-ray radius reported by Helder et al. (2013; see Figure 4(b)).

More generally, the ring fits allow a meaningful comparison between the radio and X-ray SNR radii. From Figure 4(b), the radius of the radio remnant has exceeded that of the X-ray counterpart since day $\sim$7500. This is also supported by the torus fits: Ng et al. (2009) employed the same torus model as ours to fit the X-ray data taken on 2008 April (day 7736), and found that it provides a slightly better fit than a simple ring, with a radius of $0\farcs82 \pm 0\farcs02$ and $\theta = 26^\circ \pm 3^\circ$. Both values are smaller than what we have obtained for the radio remnant at the same epoch ($0\farcs89$ and $36\fdg2$, respectively; Table 2), suggesting a smaller extent of the remnant in X-rays than in radio. This agrees with the simulation results (Jun & Norman 1996). In addition, the radio emission may partly originate from fast shocks at high latitudes that have not yet decelerated. This scenario can help explain the fact that the radio remnant has apparently expanded beyond the optical inner ring with radius $\sim0\farcs85$ (Plait et al. 1995).

Figure 4(c) shows that θ started to decrease at day $\sim$7000, as did the ratio R_2/R_1 of the ring model. The results suggest that the radio emission from lower latitudes has gradually dominated, which could be a consequence of shock interaction with the dense circumstellar medium in the equatorial ring. If the contribution of radio emission from high latitudes continues to diminish, then we would expect the radius estimates from both the torus and ring models to converge eventually.

The morphological evolution of SNR 1987A was accompanied by a reduction in the degree of surface brightness asymmetry. Since the radio remnant first emerged, the eastern lobe has always been brighter than the western one (see Figure 1), and this has been attributed to faster shocks in the east (e.g., Gaensler et al. 1997; N08). This scenario is supported by the significantly higher expansion velocities of the eastern lobe measured from radio observations at higher frequencies (Zanardo et al. 2013), and by the higher shock temperature found in the east from X-ray studies (Zhekov et al. 2009). The faster shock in the east is expected to encounter the equatorial ring, slow down, and exit the ring earlier than in the west. This would reduce the radio emissivity in the eastern rim and hence the overall brightness asymmetry. If the observed trend continues, the western hemisphere of the radio remnant may become brighter than the eastern hemisphere in a few years, as predicted by 3D simulations of the expanding remnant (T. M. Potter et al. 2013, in preparation). The same picture could also be applied to the X-ray emission, which exhibits similar variations in the projected brightness distribution (Ng et al. 2011b).

In X-rays, Helder et al. (2013) reported drastic deceleration of the SNR from 8500 km s^{-1} to 1820 km s^{-1} on day $\sim$5900. However, we do not find conclusive evidence for a similar deceleration in the radio emission. In particular, R_1 from the ring fit shows a constant expansion at 3890 km s^{-1}. For the torus fit, while Figure 4(b) suggests a break in the expansion, the coupling between the radius and θ described above makes the interpretation difficult. If the apparent break is physical, it would well match the deceleration of the reverse shock predicted by one-dimensional hydrodynamic simulations (see Figure 9 of Dewey et al. 2012). However, we believe that the break is likely caused by the decreasing trend in θ. Hence, it reflects a change of the emission geometry rather than the slowing down of the shock. Observing a deceleration of R_1 in future will confirm this picture. This also gives a prediction that once θ stops shrinking, the torus radius expansion rate should return to the same value as that measured for R_1.

7. CONCLUSION

We have studied the evolution of the radio remnant of SN 1987A using ATCA 9 GHz imaging observations taken between 1992 and 2013 and have carried out Fourier modeling on the visibility data to quantitatively measure the remnant structure. A truncated-shell torus model and an elliptical ring model were used to fit the remnant morphology. They both suggest a gradual decrease in the latitude extent of the remnant starting from day $\sim$7000, implying that the radio emission from the equatorial region has progressively dominated. This has been accompanied by a decreasing trend in the brightness asymmetry in the east–west direction. Together these could indicate a new stage of the remnant evolution, such that the forward shock has fully engulfed the entire inner ring and is now interacting with the densest part of the circumstellar medium.

As a direct comparison between the torus and ring model fits, they give similar results for most parameters, but the former

always suggests a larger radius. The discrepancy could be attributed to the projection effect or emission at high latitudes to which the torus model is more sensitive. This also leads to different expansion measurements. Although the torus fit shows a break in the expansion around day 7000 with the velocity slowing down from 4600 km s^{-1} to 2400 km s^{-1}, the ring fit indicates a constant expansion rate of 3890 km s^{-1}. We argue that the apparent break could be the result of coupling between the torus radius and opening angle. We expect in the future when the latter stays constant, both the torus and ring fits should give consistent expansion velocity. Further observations at higher resolution (with VLBI or ALMA, for example) would be useful in understanding the true 3D nature of the evolving remnant, and the time and latitude dependence of the expansion velocity.

We thank the referee for useful suggestions. The Australia Telescope Compact Array is part of the Australia Telescope, which is funded by the Commonwealth of Australia for operation as a National Facility managed by CSIRO. Parts of this research were conducted by the Australian Research Council Centre of Excellence for All-sky Astrophysics (CAASTRO) through project number CE110001020.

Facility: ATCA

REFERENCES

Blondin, J. M., Lundqvist, P., & Chevalier, R. A. 1996, ApJ, 472, 257
Burrows, C. J., Krist, J., Hester, J. J., et al. 1995, ApJ, 452, 680
Dewey, D., Dwarkadas, V. V., Haberl, F., Sturm, R., & Canizares, C. R. 2012, ApJ, 752, 103
Efron, B., & Tibshirani, R. J. 1993, An Introduction to the Bootstrap (New York: Chapman and Hall)
Gaensler, B. M., Manchester, R. N., Staveley-Smith, L., et al. 1997, ApJ, 479, 845
Gaensler, B. M., Staveley-Smith, L., Manchester, R. N., et al. 2007, in AIP Conf. Proc. 937, Supernova 1987A: 20 Years After: Supernovae and Gamma-Ray Bursters, ed. S. Immler, K. Weiler, & R. McCray (Melville, NY: AIP), 86
Gull, S. F., & Daniell, G. J. 1978, Natur, 272, 686
Helder, E. A., Broos, P. S., Dewey, D., et al. 2013, ApJ, 764, 11
Immler, S., Weiler, K., & McCray, R. (eds.) 2007, in AIP Conf. Proc. 937, Supernova 1987A: 20 Years After: Supernovae and Gamma-Ray Bursters (Melville, NY: AIP)
Jun, B.-I., & Norman, M. L. 1996, ApJ, 465, 800
Kemball, A., & Martinsek, A. 2005, AJ, 129, 1760
Lakićević, M., Zanardo, G., van Loon, J. T., et al. 2012, A&A, 541, L2
Luo, D., McCray, R., & Slavin, J. 1994, ApJ, 430, 264
Manchester, R. N., Gaensler, B. M., Staveley-Smith, L., Kesteven, M. J., & Tzioumis, A. K. 2005, ApJL, 628, L131
Manchester, R. N., Gaensler, B. M., Wheaton, V. C., et al. 2002, PASA, 19, 207
Morris, T., & Podsiadlowski, P. 2007, Sci, 315, 1103
Ng, C.-Y., Gaensler, B. M., Murray, S. S., et al. 2009, ApJL, 706, L100
Ng, C.-Y., Gaensler, B. M., Staveley-Smith, L., et al. 2008, ApJ, 684, 481 (N08)
Ng, C.-Y., Potter, T. M., Staveley-Smith, L., et al. 2011a, ApJL, 728, L15
Ng, C.-Y., Potter, T. M., Staveley-Smith, L., et al. 2011b, BAAS, 43, 20.11
Panagia, N. 1999, in IAU Symp. 190, New Views of the Magellanic Clouds, ed. Y.-H. Chu, N. Suntzeff, J. Hesser, & D. Bohlender (Cambridge: Cambridge Univ. Press), 549
Plait, P. C., Lundqvist, P., Chevalier, R. A., & Kirshner, R. P. 1995, ApJ, 439, 730
Potter, T. M., Staveley-Smith, L., Ng, C.-Y., et al. 2009, ApJ, 705, 261
Racusin, J. L., Park, S., Zhekov, S., et al. 2009, ApJ, 703, 1752
Sault, R. J., Teuben, P. J., & Wright, M. C. H. 1995, in ASP Conf. Ser. 77, Astronomical Data Analysis Software and Systems IV, ed. R. A. Shaw, H. E. Payne, & J. J. E. Hayes (San Francisco, CA: ASP), 433
Staveley-Smith, L., Briggs, D. S., Rowe, A. C. H., et al. 1993a, Natur, 366, 136
Staveley-Smith, L., Gaensler, B. M., Manchester, R. N., et al. 2007, in AIP Conf. Proc. 937, Supernova 1987A: 20 Years After: Supernovae and Gamma-Ray Bursters, ed. S. Immler, K. Weiler, & R. McCray (Melville, NY: AIP), 96
Staveley-Smith, L., Manchester, R. N., Kesteven, M. J., Tzioumis, A. K., & Reynolds, J. E. R. 1993b, PASAu, 10, 331
Staveley-Smith, L., Manchester, R. N., Kesteven, M. J., et al. 1992, Natur, 355, 147
Sugerman, B. E. K., Crotts, A. P. S., Kunkel, W. E., Heathcote, S. R., & Lawrence, S. S. 2005, ApJS, 159, 60
Suzuki, T., Shigeyama, T., & Nomoto, K. 1993, A&A, 274, 883
Tingay, S., Phillips, C., Amy, S., et al. 2009, in 8th International e-VLBI Workshop, Proceedings of Science, 100
Turtle, A. J., Campbell-Wilson, D., Manchester, R. N., Staveley-Smith, L., & Kesteven, M. J. 1990, IAUC, 5086, 2
Wilson, W. E., Ferris, R. H., Axtens, P., et al. 2011, MNRAS, 416, 832
Zanardo, G., Staveley-Smith, L., Ball, L., et al. 2010, ApJ, 710, 1515
Zanardo, G., Staveley-Smith, L., Ng, C.-Y., et al. 2013, ApJ, 767, 98
Zhekov, S. A., McCray, R., Dewey, D., et al. 2009, ApJ, 692, 1190